

# Quantitative PET image reconstruction employing nested expectation-maximization deconvolution for motion compensation



Nicolas A. Karakatsanis<sup>a,b,\*</sup>, Charalampos Tsoumpas<sup>c,b</sup>, Habib Zaidi<sup>a,d,e</sup>

<sup>a</sup> Geneva University Hospital, Division of Nuclear Medicine and Molecular Imaging, Geneva, CH-1211, Switzerland

<sup>b</sup> Translational and Molecular Imaging Institute, Icahn School of Medicine at Mount Sinai, New York, NY, 10029, USA

<sup>c</sup> University of Leeds, Division of Biomedical Imaging, 6.36 LIGHT labs, Leeds, LS2 9JT, United Kingdom

<sup>d</sup> University of Geneva, Neuroscience Center, Geneva, CH-1211, Switzerland

<sup>e</sup> University of Groningen, University Medical Center of Groningen, Department of Nuclear Medicine and Molecular Imaging, Groningen, 9700 RB, Netherlands

## ARTICLE INFO

### Article history:

Received 30 April 2016

Received in revised form

13 September 2016

Accepted 11 November 2016

### Keywords:

PET

Reconstruction

Motion compensation

Deblurring

Richardson-Lucy deconvolution

## ABSTRACT

Bulk body motion may randomly occur during PET acquisitions introducing blurring, attenuation-emission mismatches and, in dynamic PET, discontinuities in the measured time activity curves between consecutive frames. Meanwhile, dynamic PET scans are longer, thus increasing the probability of bulk motion. In this study, we propose a streamlined 3D PET motion-compensated image reconstruction (3D-MCIR) framework, capable of robustly deconvolving intra-frame motion from a static or dynamic 3D sinogram. The presented 3D-MCIR methods need not partition the data into multiple gates, such as 4D MCIR algorithms, or access list-mode (LM) data, such as LM MCIR methods, both associated with increased computation or memory resources. The proposed algorithms can support compensation for any periodic and non-periodic motion, such as cardio-respiratory or bulk motion, the latter including rolling, twisting or drifting. Inspired from the widely adopted point-spread function (PSF) deconvolution 3D PET reconstruction techniques, here we introduce an image-based 3D generalized motion deconvolution method within the standard 3D maximum-likelihood expectation-maximization (ML-EM) reconstruction framework. In particular, we initially integrate a motion blurring kernel, accounting for every tracked motion within a frame, as an additional MLEM modeling component in the image space (integrated 3D-MCIR). Subsequently, we replaced the integrated model component with a nested iterative Richardson-Lucy (RL) image-based deconvolution method to accelerate the MLEM algorithm convergence rate (RL-3D-MCIR). The final method was evaluated with realistic simulations of whole-body dynamic PET data employing the XCAT phantom and real human bulk motion profiles, the latter estimated from volunteer dynamic MRI scans. In addition, metabolic uptake rate  $K_i$  parametric images were generated with the standard Patlak method. Our results demonstrate significant improvement in contrast-to-noise ratio (CNR) and noise-bias performance in both dynamic and parametric images. The proposed nested RL-3D-MCIR method is implemented on the Software for Tomographic Image Reconstruction (STIR) open-source platform and is scheduled for public release.

© 2016 Elsevier Ltd. All rights reserved.

## 1. Introduction

Quantification and image resolution in clinical Positron Emission Tomography (PET) can be significantly affected by various types of motion occurring during data acquisition (Park et al., 2008; Daou, 2008; Liu et al., 2009). Motion-induced degradation of PET image resolution and quantification can occur in the form of (i) blurring at the interface between regions of different underlying

activity distributions, (ii) artifacts due to mismatched attenuation correction, and (iii) apparent discontinuities in the measured time activity curves (TACs) at each voxel across dynamic PET frames (Park et al., 2008; Daou, 2008; Liu et al., 2009; Picard and Thompson, 1997; Bloomfield et al., 2003). Apart from the involuntary and nearly periodic respiratory and cardiac motion, random bulk body motion is also frequently observed in the clinical setting. The latter type of motion is less predictable and may include various randomly occurring non-rigid transformations such as rolling, twisting and drifting of different parts of the subjects' body (Kolbitsch et al., 2014).

\* Corresponding author at: Translational and Molecular Imaging Institute, Icahn School of Medicine at Mount Sinai, New York, NY, 10029, USA.

E-mail address: [nikolaos.karakatsanis@unige.ch](mailto:nikolaos.karakatsanis@unige.ch) (N.A. Karakatsanis).

A factor expected to increase the likelihood of random bulk motion during PET acquisition is the total scan time associated with certain types of PET study protocols. For instance, synchronized PET/MR imaging, that is currently garnering increased clinical interest, may often involve lengthy PET acquisitions, while long series of various MR sequences are performed (Judenhofer et al., 2008). In addition, the recently introduced dynamic whole-body (WB) PET protocols for enhanced quantification may include several WB PET passes, thus requiring lengthy acquisitions (Karakatsanis et al., 2013a,b).

The majority of existing motion compensated (MC) 3D PET image reconstruction methods for non-brain data focus mainly on respiratory and cardiac motion and often neglect bulk motion. At the same time, most MC techniques rely on highly noisy gated static or dynamic PET data to “freeze” motion, assuming nearly-periodic cardio-respiratory motions. Thus, they often neglect the irregular and randomly occurring bulk body motion (Dawood et al., 2006, 2008; Qiao et al., 2006; Tsoumpas et al., 2010; Chun et al., 2012; Gigengack et al., 2012; Würslin et al., 2013; Rahmim et al., 2013a; Petibon et al., 2013; Fürst et al., 2015; Manber et al., 2015). Gated MC methods, not accounting for intra-gate motion, would ideally require as many gates as the number of individually tracked transformations within that frame, to eliminate intra-gate motion (Rahmim et al., 2013a; Fürst et al., 2015). As bulk motions are occurring randomly during a scan, such techniques may produce numerous gates of highly imbalanced statistical noise levels between them. Meanwhile, given the change of the activity distribution due to physiological or biochemical processes, motion gating in dynamic PET would have to be conducted for each of the dynamic frames independently. Consequently, an even larger number of gates may then be required.

The most common PET MC class of algorithms involve (i) independent 3D reconstruction of the gated raw PET data. The tracked motion is modeled in the form of 3D Cartesian motion vector fields (MVF) that are often derived from the 3D image registration between either the reconstructed PET gates or co-registered anatomical gates, such as synchronized 4D CT or MR acquisitions. Subsequently, (ii) the estimated MVFs are employed to transform/warp all gated PET images to a selected reference image. Finally, (iii) the transformed PET images are averaged to obtain the motion-compensated PET image. This class of gate-based post-reconstruction MC techniques, also known as registration-transformation-averaging (RTA) method, can be readily applied to 4D PET datasets as a post-reconstruction analysis tool (Dawood et al., 2006; Rahmim et al., 2013a).

However, RTA methods accept images, rather than sinograms or LM data, as input data and, thus, need to model count distributions in the image space, where noise is highly correlated and complex, due to the reconstruction process. Consequently, noise properties are often approximated with RTA algorithms, often leading to bias in the final images. Moreover, RTA algorithms rely on independent reconstruction of each gate, thereby their input suffer from poor count statistics. As a result, high noise is propagated to the final MC PET images through RTA algorithms. In fact, for a given frame of PET data, noise propagation is expected to increase with larger number of gates for that frame. As RTA methods rely on motion “freezing” within each gate, a larger number of gates is expected when non-periodic or random motions occur within a PET frame, thereby amplifying noise propagation (Rahmim et al., 2013a, 2007; Asma et al., 2006; Polycarpou et al., 2012). Consequently RTA methods may not be a robust approach for compensation of non-periodic motions.

Later, motion modeling was efficiently integrated within a multi-gated 4D maximum-likelihood expectation-maximization (ML-EM) framework to enhance MC efficiency (Qiao et al., 2006). Unlike indirect RTA, another class of methods, also known as 4D

motion compensated image reconstruction (4D-MCIR) algorithms, permit utilization of PET counts from all acquired gates to efficiently reconstruct the MC images directly from the gated PET raw data and thus substantially limit noise propagation in the MC image estimates, especially in very low count conditions. Furthermore, as the 4D-MCIR algorithms are applied directly on raw PET counts, the input data statistical noise now follows the well-characterized Poisson distribution, which can be accurately modeled, regardless of the gating scheme, thus reducing potential noise-induced resolution degradation effects in the MC image estimates (Rahmim et al., 2013a, 2007; Polycarpou et al., 2012).

Nevertheless, sinogram-based 4D-MCIR methods need to appropriately weight each PET gate, such that the actual level of statistical noise in each gate is accurately reflected and accounted during reconstruction to ensure proper EM convergence. As discussed earlier also for RTA methods, an MC approach relying only on gating to compensate for non-periodic motion may often result in relatively large number of gates of highly imbalanced noise. Although in the case of 4D-MCIR methods this may not significantly affect noise propagation, a larger number of gates will increase the demands for processing and memory resources. In addition, accurate weighting may become challenging among highly imbalanced gates, thus increasing the likelihood of erroneous MC estimates (Rahmim et al., 2013a, 2007).

Alternatively, promising list-mode (LM) MCIR algorithms have been previously proposed, capable of directly applying motion compensation at the PET coincidence lines of response (LORs), i.e. at the root of the problem (Rahmim et al., 2004, 2008; Livieratos et al., 2005; Lamare et al., 2007). However, LM PET scans may not be supported by some PET systems and LM data may not be regularly archived in clinic for retrospective analysis. Moreover, LM-based methods are relatively more computationally demanding.

In this study, we propose a new class of robust 3D maximum-likelihood expectation-maximization (MLEM) algorithms capable of motion-compensated PET image reconstruction (3D-MCIR) via image-based deconvolution from any *single* 3D PET sinogram, either from a static or a dynamic PET acquisition. The presented 3D-MCIR algorithms not only alleviate the need to directly reconstruct from LM data but also that of motion gating, thereby improving computational efficiency and future clinical adoptability. Moreover, the absence of gating allows for robust compensation of non-periodic motions, such as irregular breathing patterns or random body bulk motions. This feature can be particularly important for long PET scan time sessions, where non-periodic motions are more probable due to subject discomfort, such as for certain PET/MR and dynamic WB PET protocols.

The intra-frame motion in 3D-MCIR algorithms can be modeled as an image convolution or blurring kernel, the latter built from all individual tracked motion transformations. Initially, this kernel operator is simply integrated as an additional image-based modeling component of the 3D MLEM reconstruction to form the integrated-3D-MCIR algorithm. Nevertheless, the integrated convolution is expected to decelerate the overall MLEM convergence rate, due to the added voxel correlations induced by convolution, thus requiring a larger number of iterations to attain sufficient contrast recovery, thereby increasing the computational cost (Rahmim et al., 2013b). Moreover, as larger number of iterations is known to be associated with higher noise levels, a slower convergence may result in more noisy estimates for a given contrast level, thus potentially reducing contrast-to-noise-ratio (CNR) scores and lesion detectability in the final MC estimates.

Therefore, we ultimately replaced the integrated model component above with an iterative Richardson-Lucy (RL) image-based deconvolution algorithm that was nested within each global MLEM iteration step. Thus, the nested RL-3D-MCIR approach allows for multiple fast image-based RL motion deconvolution updates within

a single slower tomographic image update thereby accelerating the global MLEM convergence rate. Moreover, the principle of optimization transfer was employed to ensure the accelerated RL-3D-MCIR algorithm still converges to the proper global ML solution for improved CNR performance and wider clinical adoptability (Lange et al., 2000). Finally, the nested MLEM scheme permits the decoupling of the deconvolution from the tomographic number of iterations thus offering more parameters to optimize to potentially reduce the Gibbs or ring image artifacts often appearing in deconvolved images (Rahmim et al., 2013b).

The concept of nested ML-EM deconvolution is inspired by the recent clinical advent of advanced 3D PET reconstruction methods supporting point-spread function (PSF) resolution modeling in the form of an image-based nested PSF deconvolution process (Angelis et al., 2013). Here, we propose the replacement of the PSF resolution kernel with a generic motion convolution kernel, as an effective and practical solution to the motion compensation problem (Karakatsanis et al., 2014a). In fact, iterative RL motion deconvolution has been explored in the past, but only as a post-reconstruction deblurring technique (Gonzalez and Woods, 2008; Xu et al., 2011; El Naqa et al., 2006; Faber et al., 2009; Raghunath et al., 2009; Mohy-ud-Din et al., 2015). The presented method is implemented and validated in fully 3D mode on the Software for Tomographic Image Reconstruction (STIR) open-source platform (Thielemans et al., 2012), an object-oriented C++ software library, where we plan to release it openly in future.

## 2. Theory

### 2.1. Generalized motion model in image space

Each non-rigid 3D motion transformation can be expressed in the form of a set of three 3D MVFs, each along one of the three Cartesian coordinate principal directions: x, y and z. Subsequently, a warping operator can transform an original PET emission or attenuation map, the latter derived from CT or MRI, according to the three provided MVFs. When motion tracking within a static or each dynamic frame is available and synchronized with a 4D acquisition of PET or anatomical data, then the 4D data can be gated according to the tracked motion information, such that the residual motion within each gate is eliminated. Subsequently, advanced non-rigid registration techniques can be employed to estimate a set of three MVFs for each gate, describing the motion transformation between the gate and a reference space (Buerger et al., 2011).

The presented 3D MCIR PET reconstruction method is applied on ungated PET data, regardless if these PET data have been previously gated to estimate their motion contamination or the motion was tracked from synchronized 4D CT or MR data, the latter method often leading to a more robust motion estimation, if such anatomical data are available. Moreover, the proposed MCIR method can potentially model any type of generic motion combination (e.g. respiratory + cardiac + bulk + rigid) occurring within each ungated frame and is only being limited by the accuracy and precision of the motion estimates. In this study, we are focusing on the MC problem itself assuming that the 4D motion estimation is reasonably accurate. The employed forward motion model considers each motion-contaminated image as a time-weighted average of a set of motion-transformed/warped images:

$$m_{jt}(\mathbf{x}_t) = \sum_{s \in \mathcal{S}_t} c_{st} W_{j_0 \rightarrow j_s}^s(\mathbf{x}_t) \quad (1)$$

Notation:

- $W_{j_0 \rightarrow j_s}^s$  is the forward motion warping/transform operator from voxel of the original image space to voxel  $j_s$  of the motion-transformed image space for a particular  $s$  transformation,

- $\mathbf{x}_t = [x_{j_0t}]_{j_0=1}^{n_j}$  and  $\mathbf{m}_t \equiv [m_{jt}]_{j=1}^{n_j}$  are the motion-corrected and motion-contaminated images of dynamic frame  $t$ , respectively. Both images are comprised of  $n_j$  voxels in total. Note that the overall weighted averaging operation resulted in a new motion-blurred image space, denoted with voxel index  $j$ , for the  $\mathbf{m}_t$  images. The image vectors can represent either reconstructed PET or CT- or MRI-derived attenuation images. For notation simplicity we assume that all types of images are of the same dimensions in this study,
- $\mathcal{S}_t$  is the subset of motion transformations occurring during frame  $t$  and
- $c_{st}$  is the respective time-weighting factor, defined as the time fraction relative to the duration of frame  $t$ , for which the  $s \in \mathcal{S}_t$  motion transformation holds (Mohy-ud-Din et al., 2015).

The overall effect of the time-weighted averaging operation is the introduction of motion-induced blurring in each of the original motion-free dynamic PET images, which is equivalent to the effect of convolving with an image-based kernel. Thus, the presented approach can be considered directly analogous to image-based PSF recovery reconstruction algorithms except that the PSF resolution response is now replaced with a motion blurring kernel.

### 2.2. Motion deconvolution integrated within 3D ML-EM PET image reconstruction (integrated 3D MCIR)

We assume, throughout this study, a PET system with  $n_j$  detector pair bins in fully 3D acquisition mode and a reconstruction of  $n_t$  dynamic images of  $n_j$  voxels each. Initially, let us consider the conventional approach of completely integrating our generalized motion model to the PET ML-EM reconstruction framework, denoted here as *integrated* 3D-MCIR algorithm. After adding the image-based motion modeling term  $m_{jt}(\mathbf{x}_t)$  (Eq. (1)) into the ML-EM image estimation algorithm, the EM forward projection process can be described as follows:

$$\bar{y}_{it}(\mathbf{x}_t) = \sum_j p_{ijt} m_{jt}(\mathbf{x}_t) + \bar{r}_{it} \quad (2)$$

Notation:

- $\bar{\mathbf{Y}} \equiv [\bar{y}_{it}]_{i,t=1}^{n_i, n_t}$  is the expected projection data acquired during frame  $t$ ,
- $\mathbf{X} \equiv [\mathbf{x}_t]_{t=1}^{n_t}$  is the dynamic motion-compensated image vector to be estimated,
- $\bar{\mathbf{R}} \equiv [\bar{r}_{it}]_{i,t=1}^{n_i, n_t}$  is the expected scattered and random data vector at each dynamic frame  $t$  and
- $\mathbf{P}^t \equiv [p_{ijt}]_{i,j=1}^{n_i, n_j}$  is the system response matrix at frame  $t$ , with each element  $p_{ijt}$  denoting the probability of an annihilation event occurring in voxel  $j$  and being detected in sinogram bin  $i$  during frame  $t$ .

Dynamic PET ML-EM reconstruction schemes aim at maximizing the Poisson log-likelihood of the measured dynamic projection measurements  $\mathbf{Y} \equiv [y_{it}]_{i,t=1}^{n_i, n_t}$ , given the estimated dynamic image vector  $\mathbf{X}$ , with  $\mathbf{y}_t \equiv [y_{it}]_{i=1}^{n_i}$  denoting the measured projection data for  $t$ -th time frame:

$$L(\mathbf{Y}|\mathbf{X}) = \sum_t \sum_i y_{it} \log \bar{y}_{it}(\mathbf{x}_t) - \bar{y}_{it}(\mathbf{x}_t) \quad (3)$$

$$L_t(\mathbf{y}_t|\mathbf{x}_t) = \sum_i y_{it} \log \bar{y}_{it}(\mathbf{x}_t) - \bar{y}_{it}(\mathbf{x}_t) \quad (4)$$

A term independent of  $\mathbf{x}_t$  is neglected from both equations above, as it does not participate in  $\mathbf{x}_t$  the optimization w.r.t.

The ML solutions, for each frame  $t$ , are defined as those that maximize the corresponding log-likelihood in Eq. (4), as denoted below:

$$\hat{\mathbf{x}}_t = \operatorname{argmax}_{\mathbf{x}_t} L_t(\mathbf{y}_t | \mathbf{x}_t) \quad (5)$$

In this study we are focusing on ML solutions to mainly demonstrate the concept of nested EM motion deconvolution for the standard ML-EM reconstruction framework. The ML-EM algorithm theoretically converges to a motion-compensated dynamic image estimate by maximizing the log-likelihood of the measured data given that estimate according to the following conventional EM update equation:

$$x_{j_0 t}^{n+1} = \frac{x_{j_0 t}^n}{\sum_{s \in S_t} c_{st} W_{j_s \rightarrow j_0}^s} \times \sum_{s \in S_t} c_{st} W_{j_s \rightarrow j_0}^s \left\{ \sum_i p_{ijt} \frac{y_{it}}{\bar{y}_{it}(\mathbf{x}_t^n)} \right\} \quad (6)$$

where  $\mathbf{1}$  denotes a 3D uniform image matrix of ones. It is important to note that the variable  $t$  in Eq. (6) denotes the time of each dynamic frame and is constant within the equation, i.e. the above ML-EM algorithm is applied to a single dynamic frame  $t$  each time. Moreover the measured  $y_{it}$  and expected  $\bar{y}_{it}$  PET projection data of each frame  $t$  are not gated. Thus unlike the respective MLEM equation in 4D-MCIR algorithms which involve multiple PET data gates per dynamic frame (Qiao et al., 2006), the proposed MCIR method in Eq. (6) employs only a single gate for each dynamic frame, containing all PET data of that frame, thereby considered a 3D reconstruction algorithm.

The integration of motion modeling together with the forward and backward tomographic projection operations effectively adds to the algorithm the extra task of solving for an image deconvolution problem simultaneously with the tomographic problem. As the spatial correlations among the reconstructed voxels are enhanced with the added motion convolution operation, the EM algorithm now requires more iteration steps to converge to an ML solution. As noise levels are increasing with iterations, a slow convergence rate will result in more noisy images for a given contrast, thus limiting the CNR performance.

### 2.3. Nested iterative Richardson-Lucy motion deconvolution within ML-EM PET image reconstruction (nested RL-3D-MCIR)

In order to improve the convergence rate of the initial 3D-MCIR method presented above, we ultimately replaced the integrated motion modeling component with an iterative RL motion deconvolution EM algorithm, nested within each iteration step of the tomographic 3D-MLEM algorithm. In this nested 3D-MLEM

approach, denoted here as the RL-3D-MCIR algorithm, we essentially decouple the fast image-based motion EM deconvolution from the much slower tomographic MLEM estimation to allow for multiple fast motion deconvolution updates for every single but slower tomographic image update. Moreover, we employ the optimization transfer principle to ensure every nested and global update will lead towards the proper global ML solution (Lange et al., 2000). As the new scheme permits multiple faster updates for each slower one, acceleration is expected in the global convergence rate, thus improving computational and CNR performance, compared to the integrated-3D-MCIR method. The optimization transfer method has been previously applied in the form of nested ML-EM PET reconstruction algorithms supporting resolution modeling (Angelis et al., 2013) or Patlak graphical analysis (Wang and Qi, 2010, 2012; Karakatsanis et al., 2014c, 2016). In this study we employ this concept to accelerate the convergence of motion compensated PET image reconstruction while ensuring proper convergence.

In particular, the optimization transfer theory (Lange et al., 2000), is utilized to construct, at each global iteration step  $n$ , a surrogate objective function for which the MLEM optimization is simplified, while ensuring convergence to the global ML solution of Eq. (5). The resulting surrogate objective functions express the log-likelihood of a motion-contaminated  $t$ -th image frame  $\mathbf{m}_t^n$ , as estimated at global iteration step  $n$ , given a deconvolved image estimate  $\mathbf{x}_t$  of the same frame.

$$Q_{t,n}(\mathbf{m}_t^n | \mathbf{x}_t) = \sum_j \left( \sum_i p_{ijt} \right) m_{jt}^n \log m_{jt}(\mathbf{x}_t) - m_{jt}(\mathbf{x}_t) \quad (7)$$

Thus, the maximization problem of the original global log-likelihood objective function  $L_t(\mathbf{y}_t | \mathbf{x}_t)$  is now effectively transferred, at each global iteration step  $n$ , into the maximization of  $Q_{t,n}(\mathbf{m}_t^n | \mathbf{x}_t)$  a surrogate objective function

$$\mathbf{x}_t^n = \operatorname{argmax}_{\mathbf{x}_t} Q_{t,n}(\mathbf{m}_t^n | \mathbf{x}_t) \quad (8)$$

The objective functions  $Q_{t,n}$  in Eq. (7) define the optimization problem for each frame  $t$  and global iteration step  $n$ . The respective ML-EM solution  $\mathbf{x}_t^n$  is expected to converge to a global ML-EM solution  $\hat{\mathbf{x}}_t$ , such that  $L_t(\mathbf{y}_t | \hat{\mathbf{x}}_t) \geq L_t(\mathbf{y}_t | \mathbf{x}_t)$ , i.e. the measured data log-likelihood is globally maximized. The concept of optimization transfer for the nested RL-3D-MCIR approach is also graphically illustrated in Fig. 1. The global MLEM convergence is guaranteed provided the surrogate objective functions  $Q_{t,n}(\mathbf{m}_t^n | \mathbf{x}_t)$  satisfy the constraints shown in Fig. 1 (Lange et al., 2000).

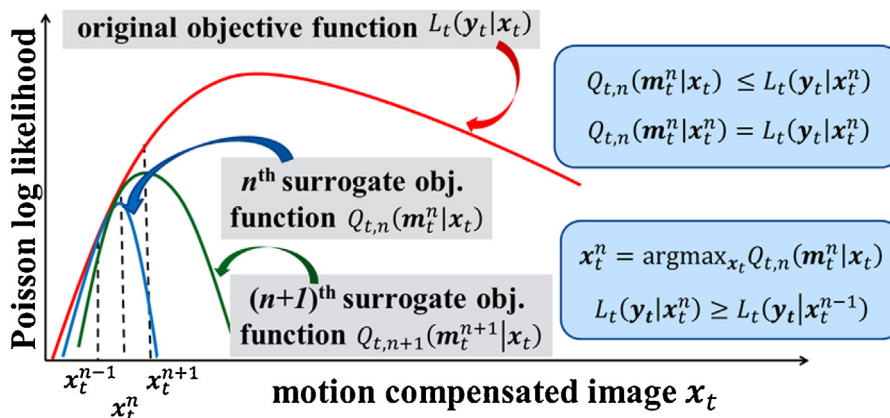


**Fig. 1.** Graphical illustration of the optimization transfer concept and the required constraints for the surrogate objective functions at two consecutive global ML-EM iteration steps. The maximization problem of the original objective function  $L_t$  (red) is transferred to the maximization of the less complex image-based surrogate objective functions  $Q_{t,n}$  and  $Q_{t,n+1}$  at  $n$  (blue) and  $n+1$  (green) global iteration steps respectively. The plots are not based on measured data and are only intended for graphical illustration of presented theoretical concepts. (For interpretation of the references to colour in this figure legend, the reader is referred to the web version of this article.)

The ML solutions for Eqs. (5) and (8) are provided by the iterative nested ML-EM algorithm, as described with Eqs. (9) and (10) below for our motion-compensated reconstruction problem. The proof for those solutions has been previously discussed in MLEM applications of the optimization transfer theory and in analogous work for nested PSF-3D-MLEM algorithms (Lange et al., 2000; Angelis et al., 2013). At global iteration step  $n$ , initially, an intermediate motion-contaminated image estimate  $\mathbf{m}_t^n$  is derived, at each  $t$ -th frame, using the measured projection data  $y_{it}$  as reference:

$$m_{jt}^n = \frac{m_{jt}(\mathbf{x}_t^{n-1})}{\sum_i p_{ijt}} \sum_i p_{ijt} \frac{y_{it}}{y_{it}(\mathbf{x}_t^{n-1})} \quad (9)$$

Subsequently, a nested Richardson-Lucy EM update equation is employed to iteratively deconvolve the motion contamination and estimate after  $k = 1, \dots, n_k$  nested EM sub-iterations, the next global motion-free image estimate  $\mathbf{x}_t^n$ , utilizing the intermediate motion-contaminated image  $\mathbf{m}_t^n$  as a reference:

$$x_{j_0 t}^{n,k+1} = \frac{x_{j_0 t}^{n,k}}{\sum_{s \in S_t} c_{st} W_{js \rightarrow j_0}^s} \sum_{s \in S_t} c_{st} W_{js \rightarrow j_0}^s \left\{ \frac{m_t^n}{m_t(\mathbf{x}_t^{n,k})} \right\}, k = 1 \dots n_k \quad (10)$$

After all  $n_k$  nested sub-iterations are completed, the derived  $\mathbf{x}_t^{n,n_k+1}$  image update is considered the next global ML motion-corrected image update  $\mathbf{x}_t^n$  that will be used as initializer for the subsequent global iteration step  $n + 2$ . Thus, using a voxel-based equation notation, we have:  $x_{jt}^{n,1} = x_{jt}^{n-1}$ ,  $x_{jt}^n = x_{jt}^{n,n_k+1}$ .

The iterative RL motion deconvolution algorithm was previously evaluated only as a post-reconstruction indirect image deblurring process (indirect-RL) (Gonzalez and Woods, 2008; Xu et al., 2011; El Naqa et al., 2006; Faber et al., 2009; Raghunath et al., 2009; Mohy-ud-Din et al., 2015). Similar to RTA methods, the indirect-RL methods are designed only for application on already reconstructed PET images. Thus, they can only approximate the highly correlated and complex noise properties of the reconstructed input image data. On the other hand, both the integrated- and RL-3D-MCIR algorithms presented here deconvolve the modeled motion in the image space at every global ML-EM iteration cycle and pass the deconvolved estimates to the next cycle, until sufficient ML-EM convergence is attained. Although the deconvolution is conducted on the image space, the actual fully 3D ML-EM reconstruction is performed directly on the projection space, where the counts and

their underlying noise follow the well-defined Poisson distribution. Thus, the proposed 3D-MCIR methods allow for more accurate modeling of the noise properties through the reconstruction process thus permitting significantly less noise-induced inaccuracies in the MC PET image estimates compared to indirect-RL schemes. This feature can be particularly important at the high noise levels usually present in low-count (Karakatsanis et al., 2007) or dynamic PET data, as is the case with WB dynamic acquisitions (Karakatsanis et al., 2013a).

### 3. Methods

#### 3.1. Dynamic WB PET acquisition protocol

Currently, the established surrogate of standardized uptake value (SUV) is primarily employed in clinical oncology to evaluate the in-vivo metabolic activity 3D spatial concentration of the administered radioactive tracer in normal and pathological tissues. However, the tracer activity concentration in the blood and its absorption from the living tissues changes dynamically with time, due to various physiological processes regulating its in-vivo biological uptake. As a result, SUV measurements are dependent on post-injection (p.i.) scan time window as well as the time course of the tracer concentration in blood plasma, the latter also known as input function (Fig. 2).

On the contrary, dynamic PET imaging, involving multiple sequential acquisition frames over time, enables tracking of the tracer activity distribution throughout the scan duration. Then, the acquired four-dimensional (4D) PET data can be analyzed utilizing graphical analysis or compartmental kinetic models, to estimate at the voxel level a range of physiological parameters of interest, such as the tracer uptake rate constant  $K_i$ , which is primarily useful in oncology for the quantitative evaluation of tumor staging and therapy response. Nevertheless, dynamic PET acquisitions have, until recently, been confined to single bed axial field-of-views (FOVs) in an effort to attain sufficient count statistics via continuous temporal sampling of single bed positions, due to relatively low or moderate overall detection efficiencies of previous scanner generations. Consequently, dynamic PET scan protocols had not been able to support WB FOVs; the latter considered a crucial protocol feature

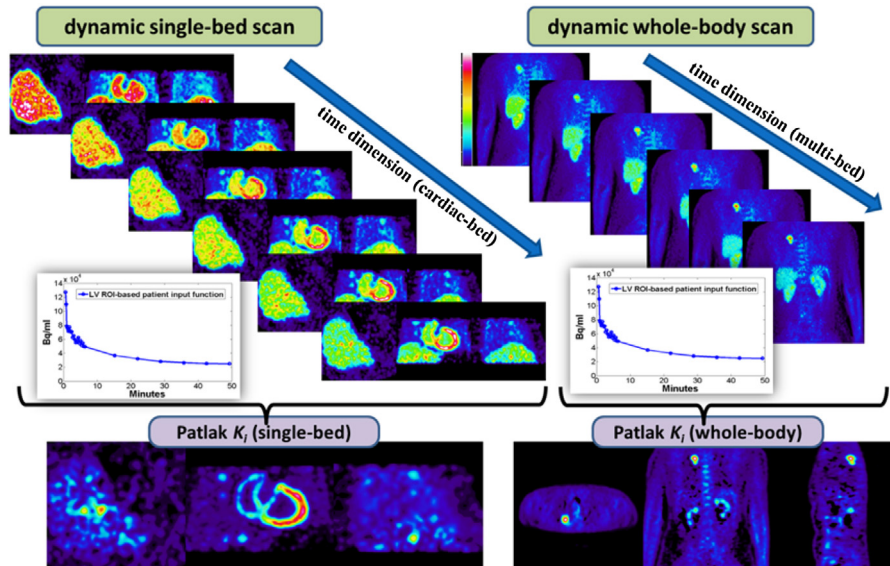
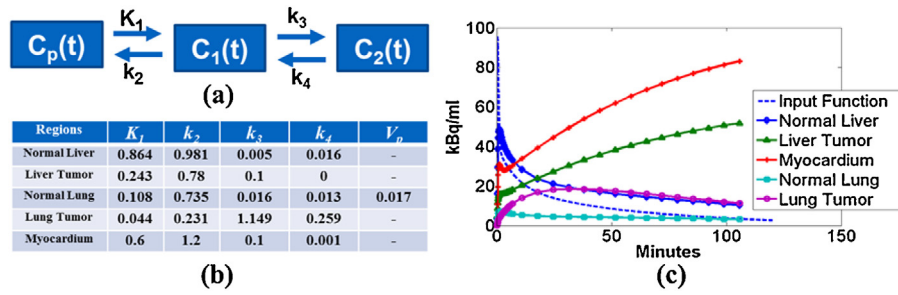


Fig. 2. Illustration of acquisition protocol for simulated single-bed (left) and clinical whole-body (right) dynamic PET imaging and the corresponding sPatlak  $K_i$  images. In both cases the image-derived input function from a heart left-ventricle region of interest is utilized for the production of the  $K_i$  parametric images.



**Fig. 3.** (a) The standard fully compartmental  $^{18}\text{F}$  FDG-PET tracer kinetic model. It consists of the  $C_p(t)$  input function compartment, as well as the tissue compartments for free-tracer  $C_1(t)$  and metabolized tracer  $C_2(t)$  concentration over post-injection time  $t$ . (b) the  $k$ -parameter values table obtained from literature for tumor and normal regions and (c) the modeled TACs assigned to the respective tumor and normal XCAT phantom regions.

for the thorough evaluation of disease spread across the body, such as potential tumor metastasis in oncology.

Recently, we proposed a clinically feasible  $^{18}\text{F}$  FDG PET parametric imaging framework (Karakatsanis et al., 2013a), capable of delivering highly quantitative WB parametric images by supporting (i) multiple PET acquisition passes over multiple beds and (ii) graphical analysis of the acquired 4D WB data using robust standard linear Patlak (sPatlak) (Karakatsanis et al., 2013b) or non-linear generalized Patlak (gPatlak) methods (Karakatsanis et al., 2015a). Although the associated total scan duration of  $\sim 30$ – $40$  min may be considered clinically feasible, such protocols are naturally expected to increase the likelihood of bulk motion during the acquisition (Karakatsanis et al., 2014b). Furthermore, we are currently evaluating a combined SUV/Patlak imaging framework based on the previous WB dynamic scan protocol (Karakatsanis et al., 2015b). In both versions, the acquisition time has to be distributed over multiple short dynamic frames of 30–45 s per bed and pass, thus amplifying the statistical noise levels in the measured data (Karakatsanis et al., 2013a, 2015a). However, in the newer protocol, the SUV image is synthesized for each bed position from multiple dynamic frames, thus increasing the likelihood of motion-degraded SUV resolution due to inter-frame misalignments (Karakatsanis et al., 2015b). Consequently, the quantitative accuracy (bias/resolution) and precision (noise) performance associated with both dynamic and parametric images may be degraded in clinical WB dynamic PET studies, due to bulk motion and high levels of statistical noise.

### 3.2. Generation of realistic kinetic 4D simulated image data

The performance of the proposed nested RL-MCIR method is evaluated on realistic 4D synthetic emission and attenuation motion-degraded data, which are acquired according to our recently introduced clinical WB dynamic PET acquisition protocol (Karakatsanis et al., 2013a). A dynamic WB protocol was preferred over simple static imaging to allow for evaluation of method performance under more challenging conditions, than those often expected in clinic, in terms of noise levels, types of motion as well as sampling of the time activity curves (TACs).

The standard kinetic model for  $^{18}\text{F}$  FDG tracer, i.e. a 2-compartment 4-kinetic parameter compartmental model (Fig. 3a), and the Feng input function model (Feng et al., 1993), were employed for the production of the simulated noise-free TACs for a range of normal tissues and tumors in the torso region (Fig. 3c). The employed kinetic parameter values in Fig. 3b, were acquired from literature review of clinical dynamic PET studies (Okazumi et al., 1992, 2009; Torizuka et al., 1995, 2000; Dimitrakopoulou-Strauss et al., 2006). Subsequently, the noise-free TACs were assigned to the respective regions of the anthropomorphic digital XCAT human torso phantom (Segars et al., 2010), limited to a Biograph mCT cardiac bed axial FOV, to generate realistic motion-free kinetic

4D XCAT phantom images. Finally, a single motion-free XCAT PET attenuation map was also created.

### 3.3. Application of real human MRI-derived body bulk motion

A series of real human body non-rigid and highly irregular motion transformations were applied to each dynamic cardiac PET image frame of the XCAT phantom. The initial motion-transformed 3D XCAT images were provided from a recently published dataset, which was created and validated by Dr. Arda Könik from human volunteer MRI scans mimicking characteristic bulk motions (Könik et al., 2014). The exercised natural 3D motion transformations were tracked with reflective markers, properly positioned on body surface, and 3D stereo optical imaging tracking techniques. Multiple combinations from a range of principal bulk transformations were applied in different combinations over the initial motion-free dynamic frames, resulting in a total of 30 different non-rigid transformations randomly distributed across the 6 cardiac frames. The following five types of body bulk motions were randomly combined: axial slide (rigid motion), lateral torso bend, shoulder twist, shoulder stretch and side roll (Könik et al., 2014).

Initially, the five basic human motion transformations above were applied to XCAT to generate five motion-transformed editions for each dynamic frame. Then a hierarchical local affine registration method<sup>6</sup> was utilized to estimate, for each of the five transformations of each frame, three MVFs, each corresponding to the x, y and z Cartesian directions, respectively. The resulting  $6 \times 5 \times 3 = 90$  MVFs were then averaged across frames to produce  $5 \times 3 = 15$  averaged MVFs of higher precision for each of the basic five principal bulk motions. Later, the new 5 sets of MVFs were randomly combined, at each x, y and z direction, to create 25 new sets of MVFs, i.e.  $n_s = 30$  MVF sets were created in the end. One characteristic set of MVFs is shown in Fig. 4. In this proof of principle study, we focused our evaluation on correction of bulk motions only and thus we chose not to introduce cardio-respiratory motion to each frame.

Subsequently, the 30 motion transformations were randomly grouped into 6 sets, as many as the dynamic frames, each denoted as  $\mathbf{s}_t$ ,  $t = 1, \dots, 6$ . Then, each set of transformation was sequentially applied, through the warping operation  $W_{j_0 \rightarrow j_s}^{\mathbf{s}_t}$ ,  $\mathbf{s}_t \in \mathbf{s}_t$ , to its corresponding motion-free frame  $\mathbf{x}_t$  to produce 30 noise-free motion-transformed 3D PET emission images  $\mathbf{d}_s$ . In addition, the same set of transformations was also applied to the single XCAT attenuation image  $\mu_0$  to produce 30 motion-transformed PET attenuation images  $\mu_s$ .

### 3.4. Simulation of 4D motion-contaminated emission and attenuation projection PET data

Initially, each motion-transformed attenuation PET image  $\mu_s$  was forward projected and the respective attenuation factor

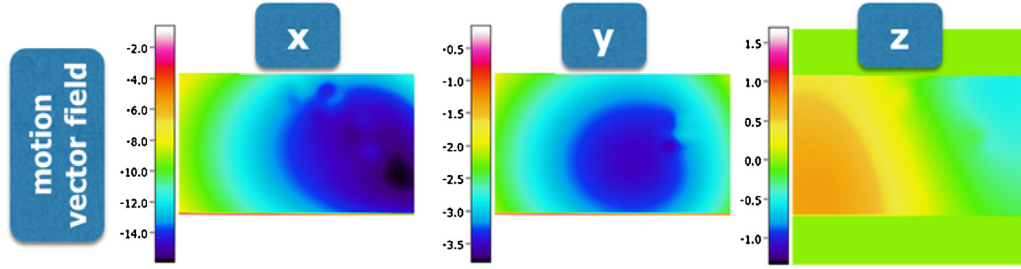


**Fig. 4.** A characteristic example of three 3D MVFs in the orthogonal Cartesian directions x, y and z, respectively. The illustrated set corresponds to one of the 30 motion transformations applied to the simulated 4D data. Each transformation is a combination of the five basic transformations, as estimated from the initial XCAT dataset. The respective 3D MVFs utilized within the RL-MCIR method differed from those applied when synthesizing the motion-contaminated 4D simulated data: the former were estimated with image registration methods between the motion transformed images. The focus of this study is on motion compensation and not motion tracking.

sinograms were calculated as:  $\mathbf{a}_s = e^{-\text{fwdproj}(\mu_s)}$ , where “fwdproj” denotes the Biograph mCT (Siemens Healthcare) PET/CT scanner fully 3D analytic forward projection operation, as implemented in STIR according to the geometric properties and sensitivity performance of the system (König et al., 2014). Subsequently, each motion-transformed PET emission image  $\mathbf{d}_s$  was forward projected, followed by application of the respective attenuation factors  $\mathbf{a}_s$  in the projection space to produce the corresponding motion-transformed attenuated noise-free emission projection data  $\mathbf{e}_s = \mathbf{a}_s \circ \text{fwdproj}(\mathbf{d}_s)$  with “ $\circ$ ” denoting a Hadamard or component-wise matrix product operation. Then, each motion-contaminated sinogram  $\mathbf{y}_t = \sum_{s \in \mathcal{S}_t} c_{st} \mathbf{e}_s$  is calculated as the time-weighted average of

the group of transformed sinograms  $\mathbf{e}_s$ ,  $s \in \mathcal{S}_t$ , corresponding to a certain frame. Scatter and random events were not added.

A total of 20 realizations of quantitative levels of Poisson noise were added to each simulated dynamic sinogram  $\mathbf{y}_t$  according to the current mean of the simulated dynamic  $^{18}\text{F}$  FDG radioactivity at each frame. The mean activity concentration was determined by the reported sensitivity performance of the Biograph mCT scanner (Jakoby et al., 2011), the  $^{18}\text{F}$  decay rate, the modeled tracer kinetics (Okazumi et al., 1992, 2009; Torizuka et al., 1995, 2000; Dimitrakopoulou-Strauss et al., 2006) and the duration  $t_s$  of each frame (Karakatsanis et al., 2013a). Later, the noise-free and noisy dynamic projections, without and with 4D motion contamination, were reconstructed using the standard 3D ML-EM algorithm in STIR (Thielemans et al., 2012). The motion-contaminated dynamic projections were also reconstructed with our proposed nested RL-3D-MCIR algorithm, as implemented in fully 3D mode within STIR v3.0. The attenuation correction factors (ACFs) sinograms  $\bar{\mathbf{a}}_t$  were derived by applying time-weighted averaging to the motion-transformed ACF sinograms  $\mathbf{a}_{s,t} \in \mathcal{S}_t$ , i.e.  $\bar{\mathbf{a}}_t = \sum_{s \in \mathcal{S}_t} c_{st} \mathbf{a}_s$ . The latter

type of averaging was preferred as we have previously concluded it minimizes the inevitable, in the absence of gated MCIR, motion-induced mismatches between emission and attenuation maps for each frame (Mohy-ud-Din et al., 2015).

Finally, all reconstructed WB dynamic frames and the measured input function  $b_t = b(\tau_t)$  at mid-frame times  $\tau_t$  were fitted with a validated multi-bed standard Patlak (sPatlak) graphical analysis method to estimate at each voxel the physiologic parameters of tracer uptake rate  $K_i$  and total blood volume distribution  $V$

according to the equation:  $x_{jt} = K_i \int_0^{\tau_t} b_t d\tau + Vb_t$  (Karakatsanis et al.,

2013b). Thus, in the end we obtained the image estimates of  $K_i$  and  $V$  sPatlak parameters.

## 4. Results

The reconstructed images corresponding to the cardiac bed from the 6 dynamic WB PET frames and the respective  $K_i$  images are presented in Figs. 5 and 6, without and with noise, respectively. The impact of human body bulk motion on the image quality is evident in both noise-free and noisy motion-contaminated dynamic and  $K_i$  images, in the absence of motion compensation. Moreover, the visual inspection of the quality of the respective MC images produced with the nested RL-3D-MCIR method suggests a partial but significant recovery of the motion-degraded image resolution for both noise-free and noisy simulated dynamic and respective parametric image data. In particular, the improvement is more apparent for the parametric  $K_i$  sPatlak images. This observation could be attributed to the higher sensitivity to motion for parametric imaging, relative to conventional static or dynamic SUV PET, due to the introduction of motion-induced voxel TAC discontinuities between subsequent dynamic PET frames. Our results suggest a significant resolution degradation of the  $K_i$  images in this case, which in turn is considerably eliminated when all frames are corrected for motion prior to Patlak analysis.

However, in the absence of noise (Fig. 5), distinct Gibbs artifacts can be also observed in both the dynamic and  $K_i$  images with the RL-3D-MCIR method. Such characteristic artifacts are expected as a result of the correlation between the voxel estimates, due to the iterative image deconvolution process. Similar artifacts can be identified in the same regions for the noisy images too (Fig. 6). Furthermore, in the presence of noise (Fig. 6), relatively higher levels of spatial noise are visually observed for the motion-compensated images, especially in regions with low uptake such as the background tissues. The presence of elevated noise levels can be attributed to the noise propagation properties of ML-EM deconvolution algorithms with increasing iterations. However, the observed noise elevation does not affect considerably the visual detectability of the simulated lesions and the CNR scores were satisfactory. In fact, we believe the nested implementation has limited noise by accelerating the convergence rate.

In addition, contrast-to-noise ratio (CNR) scores and noise vs. bias trade-off curves are evaluated in Fig. 7 for the last (6th) dynamic PET frame and the parametric  $K_i$  images. In particular, 20 noise realizations were employed and the quantitative evaluations were performed every 21 ML-EM iteration steps on lung and liver regions of interest and their respective background. The application of the RL-3D-MCIR method, involving 10 nested RL sub-iterations per global tomographic iteration step, partially recovers, for both noise-free and noisy data, the ground truth resolution of the motion-free dynamic and parametric images, with relatively greater enhancements for the latter. In addition the recovery of the resolution or, equivalently, the reduction of bias, is attained without significant noise amplification and Gibbs artifacts, as demonstrated

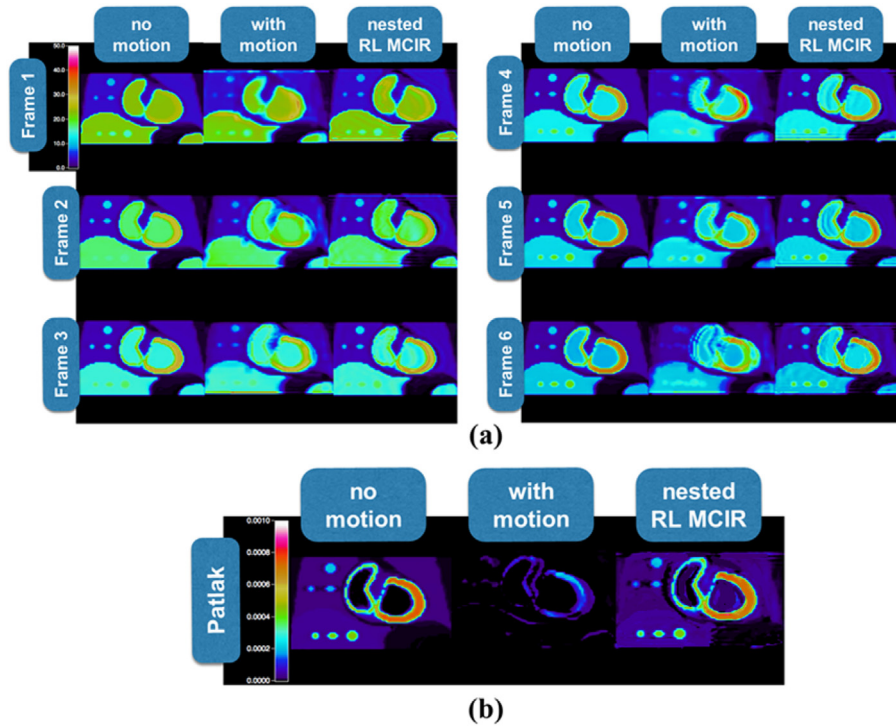


**Fig. 5.** (a) Noise-free reconstructed dynamic PET and (b) sPatlak  $K_i$  images, corresponding to the cardiac bed and to time frames of our validated clinical WB dynamic PET protocol. In all cases, motion-free, ground truth 4D data (1st column) are used as a reference to compare against motion contaminated data estimated without motion correction (2nd column) and with nested RL-3D-MCIR correction (3rd column). All PET images were reconstructed after  $4 \times 21$  ML-EM global iterations and 10 nested RL sub-iterations were employed for the RL-3D-MCIR method.

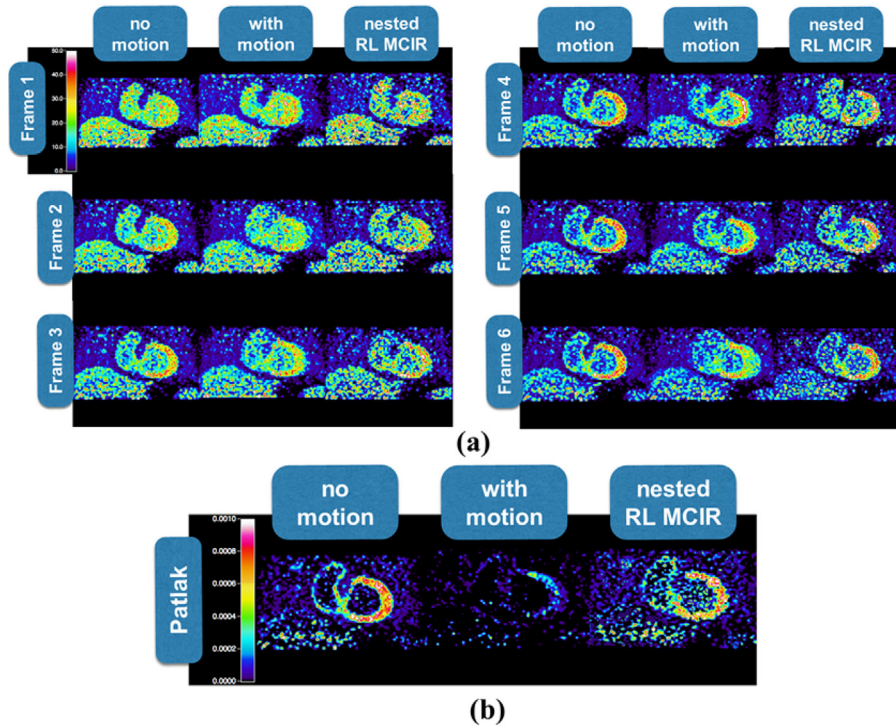


**Fig. 6.** Same type of reconstructed (a) dynamic PET and (b) sPatlak  $K_i$  images, as with Fig. 5, after adding quantitative levels of Poisson noise on projection space, equivalent to 45 s dynamic PET frames and scaled to simulate the reported sensitivity performance of Siemens Biograph™ mCT PET/CT scanner.

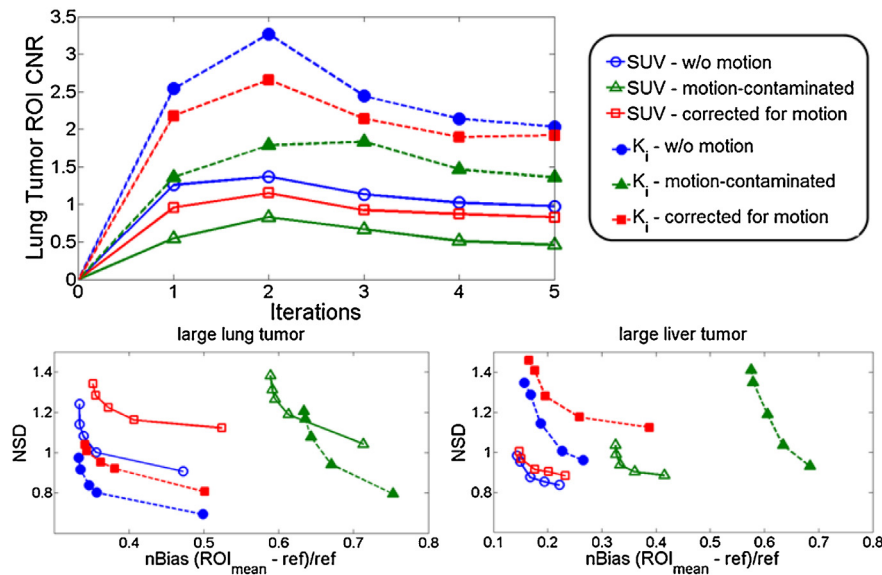


**Fig. 7.** (Top-left) Contrast-to-Noise ratios (CNRs) for lung tumor and (bottom row) noise vs. bias trade-off performance from 20 noise realizations for lung and liver tumor regions of interest, as drawn on the reconstructed PET SUV images (dotted curves), corresponding to the 6th dynamic frame, and the respective sPattak  $K_i$  images (continuous curves). The performance scores of the proposed nested RL-3D-MCIR method (red) are evaluated against the simulated motion-free ground truth images (blue) and the uncorrected for motion results (green). (For interpretation of the references to colour in this figure legend, the reader is referred to the web version of this article.)

in Fig. 6 and the respective CNR analysis in two of the lesion regions in Fig. 7.

## 5. Discussion

The 4D-MCIR methods require the partitioning of the PET data in multiple gates such that the observed intra-gate motion is negligible. Although such an approach may be suitable for the compensation of periodic motions, which are the most frequent, e.g. the cardio-respiratory motion, there exists the probability for non-periodic motions as well, such as irregular breathing patterns, or random body bulk motions. In the latter cases, a highly noisy and imbalanced set of PET gates would have been required to eliminate intra-gate motion for the 4D-MCIR methods, thus resulting in low robustness and high memory demands. Moreover, although the LM-MCIR methods would have alleviated the previous problems, they require access to LM PET data, which may not be available: in current clinical practice LM data are not regularly produced or systematically archived for retrospective analysis. Furthermore, LM-MCIR algorithms, unless they are parallelized with special software and hardware, such as GPU programming, they are associated with a high computational cost, due to the need for event-by-event processing.

Nevertheless, the integrated 3D-MCIR and RL-3D-MCIR algorithms presented here can deconvolve the tracked motion from a single sinogram PET frame, thereby alleviating the need for gating the measured PET data used in the reconstruction and for access to LM data. Their performance is thus expected to be least affected by the randomness and irregularity of motion, assuming the accuracy of the motion tracking is not affected either. As a result, the two proposed 3D-MCIR methods may exhibit higher robustness relative to the 4D-MCIR methods, when non-periodic motions are observed. Such types of motion are more probable during relatively long PET acquisitions, such as in the case of PET/MR or dynamic PET imaging. Furthermore, in the case of dynamic PET, 3D-MCIR may be preferred over 4D-MCIR methods for an additional reason: as the acquired PET data are already partitioned in short frames before motion correction, any gating scheme will result in very high noise levels.

Naturally, the performance of all MCIR methods depends on the accuracy of the tracked motion information. Therefore, both the integrated 3D-MCIR and the nested RL-3D-MCIR methods are limited by the accuracy of the estimated motion, which, in turn, depends on the gating of the 4D data employed for the tracking of the motion. Nevertheless, motion tracking does not necessarily rely on PET data gates, where the count statistics and thus noise can be very high and non-uniformly distributed across some of the gates. Instead, high resolution CT or MR anatomical 4D data can be synchronized and registered to respective PET data and subsequently gated for motion estimation purposes. In fact, nowadays, with the advent of simultaneous PET/MR scanners, motion is efficiently estimated from high resolution gated 4D MR data before employed for the motion compensation of the PET data (Fürst et al., 2015). If any random bulk or irregular cardio-respiratory motions are tracked, we recommend RL-3D-MCIR, otherwise 4D-MCIR methods may also be applied. Nevertheless, if LM PET data are available and computational resources are sufficient, then LM-MCIR could be a promising alternative approach, regardless of the type of motion tracked.

Unlike the computationally demanding event-by-event motion correction of LM-MCIR methods and the large memory needed for multiple gates processing in 4D-MCIR methods, the presented RL-3D-MCIR algorithms save both in processor and memory resources by directly applying fast convolution operations in the image space and restricting tomographic reconstruction to a single 3D sinogram. Nevertheless, it should be acknowledged that LM-MCIR methods apply motion correction at the counts level, where motion degradation effects are actually occurring. Thus, LM-MCIR algorithms are generally expected to provide the least degree of approximations in the produced MC estimates. Besides, potential CPU or GPU parallelization of LM-MCIR routines across a subset of LM events may also considerably speed-up their computation, thereby potentially enhancing their clinical adoptability in the future. However, sinogram-based reconstruction methods are so far considered more practical and have long been established in the clinical setting.

On the other hand, a limitation of both 3D-MCIR presented methods over gated 4D-MCIR and LM-MCIR algorithms is the management of the attenuation-emission mismatches due to motion. The 3D MLEM scheme of 3D-MCIR algorithms requires a *single*

attenuation correction (AC) sinogram for the reconstruction of the single motion-blurred PET frame. It is therefore inevitable that a certain degree of mismatch will exist between emission and attenuation. On the contrary, for the other two classes of methods, the attenuation is first registered to each gate or LOR, respectively. Nevertheless, we have previously conjectured that this mismatch effect is minimized on the final MC image, when choosing as the AC map the time-weighted average of all tracked motion transformations of the reference attenuation sinogram or image (Mohy-ud-Din et al., 2015).

Despite the high noise levels and the irregularity of bulk motions, RL-3D-MCIR algorithm was able to sufficiently recover the major resolution components of all six PET dynamic frames without significant noise amplification. In addition, the Patlak analysis on the RL-3D-MCIR images resulted in significant resolution recovery for the respective  $K_i$  images. In fact, the impact of motion degradation was more evident in  $K_i$  images, mainly due to inter-frame misalignments, attributed to bulk motion, and the sparse temporal sampling of the WB dynamic protocol.

Although the CNR and noise-bias trade-off performance was considerably improved with the RL-3D-MCIR method, relative to the case of no motion correction, the true contrast was not completely recovered. This observation can be attributed to the high noise levels of each dynamic PET frame and the partial volume effects in the evaluated lesion regions. Moreover, Gibbs artifacts have been also observed affecting the contrast in both noise-free and noisy images. However, the proper selection of an optimal number of nested RL iterations (10) significantly limited their effect in all cases. Nevertheless, we expect further improvements in attained resolution recovery for more common clinical conditions, such as for static or single-bed dynamic protocols, as noise levels are then significantly lower.

## 6. Conclusions

Inspired from analogous algorithms aiming at PSF resolution modeling within PET image reconstruction, we proposed a robust 3D MLEM PET image reconstruction framework capable of compensating for both periodic and non-periodic motion within a single 3D PET sinogram frame. The tracked intra-frame motion is utilized to construct an image-based motion blurring kernel that is later integrated within the 3D MLEM algorithm to effectively deconvolve the motion from the respective PET frame (integrated 3D-MCIR). Ultimately, to accelerate the global convergence rate, the integrated motion model component is replaced with an iterative Richardson-Lucy EM motion deconvolution algorithm, nested within each global MLEM iteration step (RL-3D-MCIR).

The qualitative and quantitative analysis of SUV and parametric PET images demonstrated significant recovery of the motion-degraded image contrast, without considerable noise amplification, for the proposed RL-3D-MCIR algorithm. The evaluation was performed on realistic PET data, as obtained from WB dynamic simulations with human motion profiles (Karakatsanis et al., 2013a).

Both 3D-MCIR methods are applicable to (a) static and dynamic single 3D PET frames, and (b) any traceable sequence of periodic or non-periodic motion. In addition, the accelerated RL-3D-MCIR algorithm achieves (i) superior CNR performance, for improved lesion detectability, and (ii) better processing and memory resources utilization, for wide clinical adoptability. Therefore, in the presence of non-periodic motion, the RL-3D-MCIR method is recommended, over 4D or LM-based MCIR algorithms, for its robustness and computational efficiency.

## Acknowledgments

This article is based upon work from the Action TD1007 (PET-MRI) supported by the European Cooperation in Science and Technology (COST). The presented study was funded by the Swiss National Science Foundation under grant SNSF 31003A-149957 and the Swiss Cancer Research Foundation under Grant KFS-3855-02-2016.

## References

- Angelis, G.I., Reader, A.J., Markiewicz, P.J., Kotasidis, F.A., Lionheart, W.R., Matthews, J.C., 2013. Acceleration of image-based resolution modelling reconstruction using an expectation maximization nested algorithm. *Phys. Med. Biol.* 58, 5061–5083.
- Asma, E., Manjeshwar, R., Thielemans, K., 2006. Theoretical comparison of motion correction techniques for PET image reconstruction. *IEEE Nucl. Sci. Symp. Med. Imaging Conf.* 3, 1762–1767.
- Bloomfield, P.M., Spinks, T.J., Reed, J., Schnorr, L., Westrip, A.M., Livieratos, L., et al., 2003. The design and implementation of a motion correction scheme for neurological PET. *Phys. Med. Biol.* 48, 959–978.
- Buerger, C., Schaeffter, T., King, A.P., 2011. Hierarchical adaptive local affine registration for fast and robust respiratory motion estimation. *Med. Imaging Anal.* 15, 551–564.
- Chun, S.Y., Reese, T.G., Ouyang, J., Guerin, B., Catana, C., Zhu, X., et al., 2012. MRI-based nonrigid motion correction in simultaneous PET/MRI. *J. Nucl. Med.* 53, 1284–1291.
- Daou, D., 2008. Respiratory motion handling is mandatory to accomplish the high-resolution PET destiny. *Eur. J. Nucl. Med. Mol. Imaging* 35, 1961–1970.
- Dawood, M., Lang, N., Jiang, X., Schäfers, K.P., 2006. Lung motion correction on respiratory gated 3-D PET/CT images. *IEEE Trans. Med. Imaging* 25, 476–485.
- Dawood, M., Büther, F., Jiang, X., Schäfers, K.P., 2008. Respiratory motion correction in 3-D PET data with advanced optical flow algorithms. *IEEE Trans. Med. Imaging* 27, 1164–1175.
- Dimitrakopoulou-Strauss, A., Georgoulas, V., Eisenhut, M., Herth, F., Koukouraki, S., Macke, H., et al., 2006. Quantitative assessment of SSTR2 expression in patients with non-small cell lung cancer using 68 Ga-DOTATOC PET and comparison with 18 F-FDG PET. *Eur. J. Nucl. Med. Mol. Imaging* 33, 823–830.
- El Naqa, I., Low, D.A., Bradley, J.D., Vici, M., Deasy, J.O., 2006. Deblurring of breathing motion artifacts in thoracic PET images by deconvolution methods. *Med. Phys.* 33, 3587–3600.
- Fürst, S., Grimm, R., Hong, I., Souvatzoglou, M., Casey, M.E., Schwaiger, M., et al., 2015. Motion correction strategies for integrated PET/MR. *J. Nucl. Med.* 56, 261–269.
- Faber, T.L., Raghunath, N., Tudorascu, D., Votaw, J.R., 2009. Motion correction of PET brain images through deconvolution: I. Theoretical development and analysis in software simulations. *Phys. Med. Biol.* 54, 797–811.
- Feng, D., Huang, S.C., Wang, X., 1993. Models for computer simulation studies of input functions for tracer kinetic modeling with positron emission tomography. *Int. J. Biomed. Comp.* 32, 95–110.
- Gigengack, F., Ruthotto, L., Burger, M., Wolters, C.H., Jiang, X., Schäfers, K.P., 2012. Motion correction in dual gated cardiac PET using mass-preserving image registration. *IEEE Trans. Med. Imaging* 31, 698–712.
- Gonzalez, R.C., Woods, R.E. *Digital Image Processing*, Nueva Jersey, 2008.
- Jakoby, B.W., Bercier, Y., Conti, M., Casey, M.E., Bendriem, B., Townsend, D.W., 2011. Physical and clinical performance of the mCT time-of-flight PET/CT scanner. *Phys. Med. Biol.* 56, 2375–2389.
- Judenhofer, M.S., Wehrl, H.F., Newport, D.F., Catana, C., Siegel, S.B., Becker, M., et al., 2008. Simultaneous PET-MRI: a new approach for functional and morphological imaging. *Nat. Med.* 14, 459–465.
- König, A., Connolly, C.M., Johnson, K.L., Dasari, P., Segars, P., Pretorius, P.H., et al., 2014. Digital anthropomorphic phantoms of non-rigid human respiratory and voluntary body motion for investigating motion correction in emission imaging. *Phys. Med. Biol.* 59, 3669–3682.
- Karakatsanis, N., Bao, Q., Vu, N., Chatziioannou, A., 2007. Investigation of the minimum detectable activity level of a preclinical LSO PET scanner. *2007 IEEE Nuclear Science Symposium Conference Record Vol. 4*, 3133–3138.
- Karakatsanis, N.A., Lodge, M.A., Tahari, A.K., Zhou, Y., Wahl, R.L., Rahmim, A., 2013a. Dynamic whole-body PET parametric imaging: I. Concept, acquisition protocol optimization and clinical application. *Phys. Med. Biol.* 58, 7391–7418.
- Karakatsanis, N.A., Lodge, M.A., Zhou, Y., Wahl, R.L., Rahmim, A., 2013b. Dynamic whole-body PET parametric imaging: II. Task-oriented statistical estimation. *Phys. Med. Biol.* 58, 7419–7445.
- Karakatsanis, N.A., Tsoumpas, C., Zaidi, H., 2014a. Generalized 3D and 4D motion compensated whole-body PET image reconstruction employing nested EM deconvolution. *IEEE Conf. Imag. Syst. Tech.*, 263–268.
- Karakatsanis, N.A., Lodge, M.A., Casey, M.E., Zaidi, H., Rahmim, A., 2014b. Impact of acquisition time-window on clinical whole-body PET parametric imaging. In: *IEEE Nucl. Sci. Symp. Med. Imaging Conf.*, Seattle, WA, USA, pp. 1–8, <http://dx.doi.org/10.1109/NSSMIC.2014.7430770>.
- Karakatsanis, N.A., Casey, M.E., Lodge, M.A., Rahmim, A., Zaidi, H., 2014c. Whole-body PET parametric imaging employing direct 4D nested

- reconstruction and a generalized non-linear Patlak model. *SPIE Medical Imaging*, 90330Y-90330Y.
- Karakatsanis, N.A., Zhou, Y., Lodge, M.A., Casey, M.E., Wahl, R.L., Zaidi, H., et al., 2015a. Generalized whole-body Patlak parametric imaging for enhanced quantification in clinical PET. *Phys. Med. Biol.* 60, 8643–8673.
- Karakatsanis, N., Lodge, M., Zhou, Y., Casey, M., Wahl, R., Subramaniam, R., et al., 2015b. Novel multi-parametric SUV/Patlak FDG-PET whole-body imaging framework for routine application to clinical oncology. *J Nucl. Med.* 56, 625.
- Karakatsanis, N.A., Casey, M.E., Lodge, M.A., Rahmim, A., Zaidi, H., 2016. Whole-body direct 4D parametric PET imaging employing nested generalized Patlak expectation–maximization reconstruction. *Phys. Med. Biol.* 61 (15), 5456–5485.
- Kolbitsch, C., Prieto, C., Tsoumpas, C., Schaeffter, T., 2014. A 3D MR-acquisition scheme for nonrigid bulk motion correction in simultaneous PET-MR. *Med. Phys.* 41, 082304.
- Lamare, F., Carbayo, M.L., Cresson, T., Kontaxakis, G., Santos, A., Le Rest, C.C., et al., 2007. List-mode-based reconstruction for respiratory motion correction in PET using non-rigid body transformations. *Phys. Med. Biol.* 52, 5187–5204.
- Lange, K., Hunter, D.R., Yang, I., 2000. Optimization transfer using surrogate objective functions. *J. Comput. Graph. Stat.* 9, 1–20.
- Liu, C., Pierce II, L.A., Alessio, A.M., Kinahan, P.E., 2009. The impact of respiratory motion on tumor quantification and delineation in static PET/CT imaging. *Phys. Med. Biol.* 54, 7345–7362.
- Livieratos, L., Stegger, L., Bloomfield, P.M., Schafers, K., Bailey, D.L., Camici, P.G., 2005. Rigid-body transformation of list-mode projection data for respiratory motion correction in cardiac PET. *Phys. Med. Biol.* 50, 3313–3322.
- Manber, R., Thielemans, K., Hutton, B.F., Barnes, A., Ourselin, S., Arridge, S., et al., 2015. Practical PET respiratory motion correction in clinical PET/MR. *J. Nucl. Med.* 56, 890–896.
- Mohy-ud-Din, H., Karakatsanis, N.A., Willis, W., Tahari, A.K., Wong, D.F., Rahmim, A., 2015. Intra-frame motion compensation in multi-frame brain PET imaging. *Front. Biomed. Technol.* 2, 60–72.
- Okazumi, S., Isono, K., Enomoto, K., Kikuchi, T., Ozaki, M., Yamamoto, H., et al., 1992. Evaluation of liver tumors using fluorine-18-fluorodeoxyglucose PET: characterization of tumor and assessment of effect of treatment. *J. Nucl. Med.* 33, 333–339.
- Okazumi, S., Dimitrakopoulou-Strauss, A., Schwarzbach, M., Strauss, L., 2009. Quantitative, dynamic 18F-FDG-PET for the evaluation of soft tissue sarcomas: relation to differential diagnosis, tumor grading and prediction of prognosis. *Hel. J. Nucl. Med.* 12, 223–228.
- Park, S.J., Ionascu, D., Killoran, J., Mamede, M., Gerbaudo, V.H., Chin, L., et al., 2008. Evaluation of the combined effects of target size, respiratory motion and background activity on 3D and 4D PET/CT images. *Phys. Med. Biol.* 53, 3661.
- Petibon, Y., Ouyang, J., Zhu, X., Huang, C., Reese, T.G., Chun, S.Y., et al., 2013. Cardiac motion compensation and resolution modeling in simultaneous PET-MR: a cardiac lesion detection study. *Phys. Med. Biol.* 58, 2085–2102.
- Picard, Y., Thompson, C.J., 1997. Motion correction of PET images using multiple acquisition frames. *IEEE Trans. Med. Imaging* 16, 137–144.
- Polycarpou, I., Tsoumpas, C., Marsden, P.K., 2012. Analysis and comparison of two methods for motion correction in PET imaging. *Med. Phys.* 39, 6474–6483.
- Qiao, F., Pan, T., Clark Jr., J.W., Mawlawi, O.R., 2006. A motion-incorporated reconstruction method for gated PET studies. *Phys. Med. Biol.* 51, 3769–3783.
- Raghunath, N., Faber, T.L., Suryanarayanan, S., Votaw, J.R., 2009. Motion correction of pet brain images through deconvolution: II. Practical implementation and algorithm optimization. *Phys. Med. Biol.* 54, 813–829.
- Rahmim, A., Bloomfield, P., Houle, S., Lenox, M., Michel, C., Buckley, K.R., et al., 2004. Motion compensation in histogram-mode and list-mode em reconstructions: beyond the event-driven approach. *IEEE Trans. Nucl. Sci.* 51, 2588–2596.
- Rahmim, A., Rousset, O., Zaidi, H., 2007. Strategies for motion tracking and correction in PET. *PET Clin.* 2, 251–266.
- Rahmim, A., Dinelle, K., Cheng, J.C., Shilov, M.A., Segars, W.P., Lidstone, S.C., et al., 2008. Accurate event-driven motion compensation in high-resolution PET incorporating scattered and random events. *IEEE Trans. Med. Imaging* 27, 1018–1033.
- Rahmim, A., Tang, J., Zaidi, H., 2013a. Four-dimensional image reconstruction strategies in cardiac-gated and respiratory-gated PET imaging. *PET Clin.* 8, 51–67.
- Rahmim, A., Qi, J., Sossi, V., 2013b. Resolution modeling in PET imaging: theory, practice, benefits, and pitfalls. *Med. Phys.* 40, 064301.
- Segars, W.P., Sturgeon, G., Mendonca, S., Grimes, J., Tsui, B.M., 2010. 4D XCAT phantom for multimodality imaging research. *Med. Phys.* 37, 4902–4915.
- Thielemans, K., Tsoumpas, C., Mustafovic, S., Beisel, T., Aguiar, P., Dikaio, N., et al., 2012. STIR: software for tomographic image reconstruction release 2. *Phys. Med. Biol.* 57, 867–883.
- Torizuka, T., Tamaki, N., Inokuma, T., Magata, Y., Sasayama, S., Yonekura, Y., et al., 1995. In vivo assessment of glucose metabolism in hepatocellular carcinoma with FDG-PET. *J. Nucl. Med.* 36, 1811–1817.
- Torizuka, T., Nobezawa, S., Momiki, S., Kasamatsu, N., Kanno, T., Yoshikawa, E., et al., 2000. Short dynamic FDG-PET imaging protocol for patients with lung cancer. *Eur. J. Nucl. Med.* 27, 1538–1542.
- Tsoumpas, C., Mackewn, J.E., Halsted, P., King, A.P., Buerger, C., Totman, J.J., et al., 2010. Simultaneous PET-MR acquisition and MR-derived motion fields for correction of non-rigid motion in PET. *Ann. Nucl. Med.* 24, 745–750.
- Wang, G., Qi, J., 2010. Acceleration of the direct reconstruction of linear parametric images using nested algorithms. *Phys. Med. Biol.* 55 (5), 1505–1517.
- Wang, G., Qi, J., 2012. An optimization transfer algorithm for nonlinear parametric image reconstruction from dynamic PET data. *IEEE Trans. Med. Imaging* 31 (10), 1977–1988.
- Würslin, C., Schmidt, H., Martirosian, P., Brendle, C., Boss, A., Schwenzer, N.F., et al., 2013. Respiratory motion correction in oncologic PET using T1-weighted MR imaging on a simultaneous whole-body PET/MR system. *J. Nucl. Med.* 54, 464–471.
- Xu, Q., Yuan, K., Ye, D., 2011. Respiratory motion blur identification and reduction in ungated thoracic PET imaging. *Phys. Med. Biol.* 56, 4481–4498.